Aqueous Asymmetric Supercapacitors with Pyrenetetraone-Derived Pseudocapacitive Polymer-Functionalized Graphene Cathodes Enabling a

N.B. When citing this work, cite the original published paper.

(article starts on next page)

RESEARCH ARTICLE

ADVANCED
ENERGY & SUSTAINABILITY
RESEARCH
Open Access
www.advenergysustres.com

Aqueous Asymmetric Supercapacitors with Pyrenetetraone-Derived Pseudocapacitive Polymer-Functionalized Graphene Cathodes Enabling a 1.9 V Operating Window

*Cheng Peng, Cong Guo, Yu Wang, Yafei Li, and Xiaoyan Zhang**

Pseudocapacitive polymers have garnered significant attention in the realm of supercapacitors due to their versatile molecular design capabilities, cost-effectiveness, and impressive electrical conductivity. However, limited by the low capacity and short cycle life, the investigation on conducting polymers for potential electrode materials is still insufficient. Herein, a series of pyrenetetraone-derived polymers with pyrazine units are designed and synthesized. Furthermore, UV–vis spectroscopy demonstrates the different interaction behavior between the polymers and reduced graphene oxide (rGO), which can further indicate the performance difference of the composite electrodes. As a result, the pseudocapacitive polymer/rGO composite electrode (2/1 PPYT/rGO) exhibits a high specific capacitance of 591 F g^{-1} at 1 A g^{-1} in a 1 M sulfuric acid electrolyte. The asymmetric supercapacitor (ASC) assembled by the 2/1 PPYT/rGO cathode and the annealed Ti$_3$C$_2$T$_x$ anode (2/1 PPYT/rGO//A-Ti$_3$C$_2$T$_x$) delivers an excellent energy density of 38.1 Wh kg^{-1} at a power density of 950 W kg^{-1}. Additionally, both devices demonstrate outstanding stability, retaining over 90% of their capacity after 15 000 charge/discharge cycles. As a result, these carefully engineered organic polymers, with their well-thought-out structural designs, showcase exceptional electrochemical performance, positioning them as highly promising candidates for the next generation of high-performance energy storage materials.

C. Peng, X. Zhang
Department of Chemistry and Chemical Engineering
Chalmers University of Technology
Kemigården 4, SE-412 96 Göteborg, Sweden
E-mail: xiaoyan.zhang@chalmers.se

C. Guo, Y. Wang, Y. Li
Jiangsu Collaborative Innovation Centre of Biomedical Functional Materials
School of Chemistry and Materials Science
Nanjing Normal University
Nanjing 210023, P. R. China

1. Introduction

With the increasing demand for portable consumer electronics and electric vehicles, various energy storage devices have been continuously explored by many researchers.[1–6] Among them, aqueous supercapacitor is a kind of safe, durable power supply with high power density, long lifespan, and low cost.[7–11] Compared with batteries, the widespread use of aqueous supercapacitors has been restricted due to the narrow voltage window brought by water thermodynamic decomposition voltage ($\approx$1.23 V).[12] Since energy density (E) is proportional to the square of potential window (V) and specific capacitance (C) of an electrode material according to the formula $E = 1/2CV^2$. To address this issue, strategies include but are not limited to electrolyte engineering,[13–15] surface optimization of electrodes,[16] chemical functionalization of carbon-based materials,[17] and constructing asymmetric supercapacitors (ASCs),[9,18] are employed to expand the operation window. Among them, ASCs are designed with two different electrode materials, which can cover a wider potential window to maximize the working voltage of the full cell.[19,20] Therefore, the exploration of novel electrode materials possessing high specific capacitance and wide operating window has emerged as the most sought-after research topic in the advancement of supercapacitor devices.

Graphene, the most extensively researched 2D material, shows exceptional properties such as high specific surface area, outstanding thermal and electrical conductivity, and excellent chemical stability. These unique features render it suitable for diverse applications in electronic devices, energy conversion and storage, as well as nanocomposites.[21–25] For graphene, the energy storage mechanism is dominated by adsorption/desorption of charged ions.[26] In contrast to carbon-based materials, pseudocapacitive materials such as metal oxide (RuO$_2$,[27] Bi$_2$O$_3$,[28] MnO$_2$,[29] and V$_2$O$_5$[30] etc.), redox organic molecules (quinones,[31] tetrones,[32] porphyrins[33]), and conductive polymers (PANI,[34,35] PEDOT[36]) have been employed as the promising electrode materials due to the rapid near-surface faradaic redox reactions, which may contribute to an excellent energy density. While being able to provide large energy density, metal oxides

and small organic molecules are normally struggling with a low rate performance which is caused by the limited electrical conductivity. The chemical reversibility is restricted by its dissolution into the electrolyte during the galvanostatic charge and discharge (GCD) process.[37,38] Compared with these materials, conductive polymers have drawn much attraction due to their design flexibility, low cost, and tunable properties.[39–41] Functionalization of graphene with conductive polymers endows electrode materials with high specific area, excellent electrical conductivity, and abundant redox-active sites. Compared with covalent approach, noncovalent functionalization is preferable since it does not disrupt the π system of the graphene template. This allows for the preservation of graphene's electrical conductivity to a large extent while still enabling fast charge transfer through π–π interactions. However, traditional conductive polymers such as polyaniline, polypyrrole, and polythiophene, which are used as electrode materials for supercapacitors also suffer from the limited cycle life,[42] which is caused by the irreversible redox reactions[43] and swelling and shrinking of the electrode material during the charge/discharge process.[44,45] For example, a polyaniline/reduced graphene oxide (rGO) nanocomposite-based supercapacitor device only shows a capacitance retention of ≈81% after 2000 cycles.[42] Thus, constructing novel conducting polymers with aromatic redox units can be a promising solution to address these challenges. On the one hand, anchoring conducting polymers onto graphene restricts the volume change of the conducting polymers.[46] On the other hand, the chemical reversibility of the redox sites is enhanced by the aromatic system within the conducting polymers. Furthermore, establishing the structure–property relationship of the conductive polymers will not only aid in the rational design of the polymer structures, but also facilitate an understanding of the interaction between the components of the electrode materials.[47] Pyrazine is an electron-deficient, rigid, and planar aromatic unit with a pair of C=N double bonds which is considered as cathodic materials for supercapacitor and batteries.[48,49] The planar aromatic imine structure guarantees a good π–π interaction between the conductive polymer and graphene, greatly enhancing the chemical stability of the electrode material due to the rearomatization during the redox process.[50,51] Therefore, a rational design of conductive polymers incorporating pyrazine units can not only yield excellent electrochemical performance and extended cycle life but also contribute to a deep understanding of the interactions within the composite materials.

2D titanium carbides, with a general formula of $Ti_{n+1}C_nT_x$, are selected as the anode to match with the polymer/graphene composite cathode due to its metallic conductivity and oxide-like surface, which allows fast redox reactions at anodic oxidation potential.[52–56] Hence, ASC is assembled using conductive polymer/rGO nanocomposite as the cathode and $A\text{-}Ti_3C_2T_x$ as the anode, which can provide excellent energy density and power density.

In this work, we have designed and synthesized a series of conductive polymers which contain pyrazines via condensation reactions between 4,5,9,10-pyrenetetrone and various tetramine compounds (Figure S1, Supporting Information). These polymers show different behavior when interacting with graphene due to their varying structures and properties, which can subsequently affect the electrochemical performance of the composite electrodes (**Scheme 1**). As a result, the 2/1 PPYTQ/rGO electrode shows a high specific capacitance at 603 F g^{-1}, while the 2/1 PPYT/rGO electrode shows a specific capacitance at 591 F g^{-1}. With the $A\text{-}Ti_3C_2T_x$ anode, the 2/1 PPYT/rGO//$A\text{-}Ti_3C_2T_x$ can deliver an excellent energy density of 38.1 Wh kg^{-1} at a power density of 950 W kg^{-1}. The 2/1 PPYTQ/rGO//$A\text{-}Ti_3C_2T_x$ device
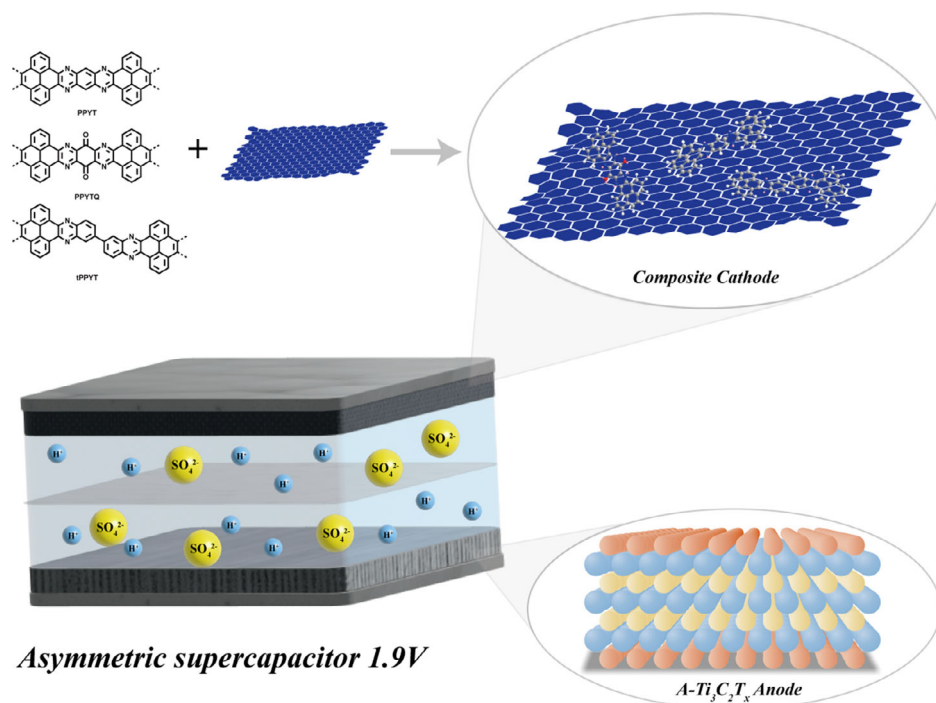
Scheme 1. Schematic diagram of aqueous ASC using conductive polymer/rGO nanocomposite as the cathode and $A\text{-}Ti_3C_2T_x$ as the anode.

can deliver an energy density of 32.1 Wh kg^{-1} at a power density of 950 W kg^{-1}.

2. Results

2.1. Material Characterization of the Cathode

The surface morphology and microstructure of the polymer and composite samples were characterized by scanning electron microscopy (SEM). The rGO shows smooth, wavy nanosheets ranging from several micrometers to more than 10 μm (Figure S2, Supporting Information). In the solid state, the pure PPYT polymer exhibits an irregular particle shape with varying sizes (Figure S3a, Supporting Information). The same scenario can also be observed in the cases of PPYTQ and tPPYT, where irregular particle shapes and various sizes are observed in the solid-state (Figure S3b,c, Supporting Information). However, when combined with the polymer, the rGO can retain its sheet-like structure while being enveloped by the pseudocapacitive polymers, indicating that the mixing process with the polymers does not disrupt the structure of the rGO (Figure S3d,e,f,

Supporting Information). The average molecular weight (Mw) of the dissolved part in dimethyl sulfoxide for PPYT and PPYTQ is 39 277 and 43 906 Da, respectively (Figure S4a,b, Supporting Information), which was obtained from gel permeation chromatography. Both of the polymers show a high degree of polymerization. Due to the very poor solubility of tPPYT in solvents, its Mw cannot be determined.

Fourier-transform infrared and UV–vis absorption spectroscopy were utilized to verify the interactions between the pseudocapacitive polymers and the rGO. The IR spectra of the PPYT, PPYTQ, tPPYT polymers, and the corresponding nanocomposite with the rGO at a ratio of 2/1, are shown in **Figure 1**a. The peaks at 1678 and 1281 cm^{-1} can be attributed to the C=N stretching from the pyrazine unit in the PPYT polymer and the bending of the C-H bonds, respectively.[57,58] Similar peaks can be observed at 1681 and 1253 cm^{-1} for the tPPYT polymer, and at 1670 and 1280 cm^{-1} for the PPYTQ polymer. These peaks correspond to the stretching of the C=N bond in the pyrazine unit and the bending of the C−H bonds in each respective polymer. Furthermore, in the case of the PPYTQ, the peak associated with the stretching of the carbonyl group overlaps with the C=N
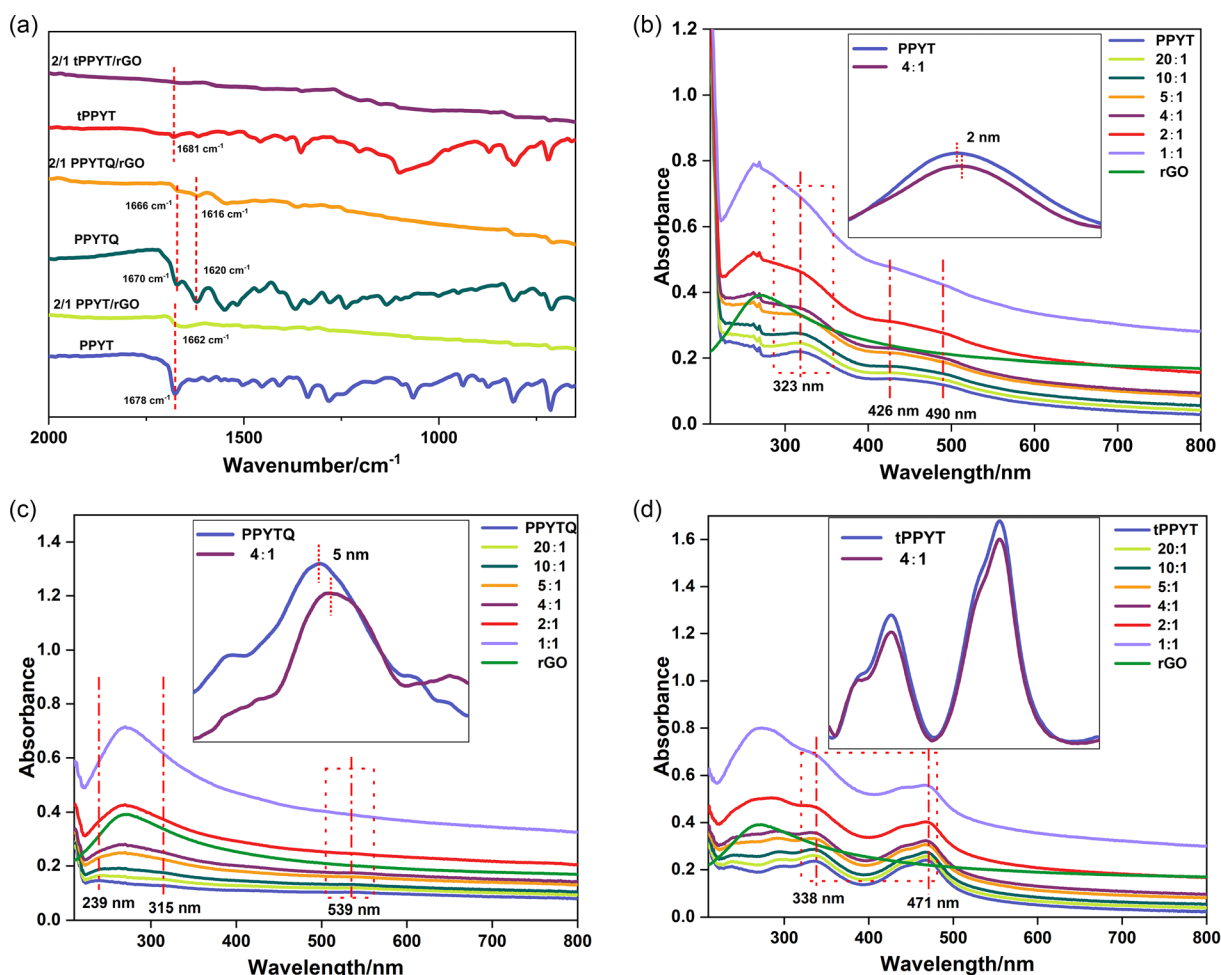

Figure 1. Infrared and UV–vis absorption spectra of the polymers and their nanocomposites with the rGO. a) IR spectra of the PPYT, PPYTQ, tPPYT polymers, and the corresponding 2/1 nanocomposites with the rGO. b,c,d) UV–vis absorption spectra of a titration between 0.1 mg mL^{-1} rGO and 0.01 mg mL^{-1} PPYT, PPYTQ, and tPPYT in ethanol. The ratio shown in the legend is polymer/rGO.

stretching peak, resulting in a broad peak observed at $\approx 1700\,cm^{-1}$. For comparison, the 2/1 PPYT/rGO composite exhibits a broad C=N stretching peak at $1662\,cm^{-1}$, indicating a $14\,cm^{-1}$ shift due to the π–π interaction between the PPYT and the rGO. Additionally, the intensity of the absorption peaks in the nanocomposites is weaker compared to the PPYT. The decrease in the intensity can be attributed to the confined vibrations of the functional groups on the PPYT within the nanocomposite.[59] A similar phenomenon can also be observed for the 2/1 PPYTQ/rGO nanocomposite, which shows a $4\,cm^{-1}$ shift of the C=N peak. In contrast, no significant absorption peak can be observed in the IR spectrum of the 2/1 tPPYT/rGO nanocomposite.

The interaction between the three PYT-based polymers and the rGO is further investigated through UV−vis spectrophotometric titration in ethanol (Figure 1b–d). As a reference, the rGO exhibits an absorption band at a wavelength of $\approx 271\,nm$ which can be attributed to the π–π^* transitions of the C=C double bonds.[60] For the PPYT polymer, it shows a strong absorption band at 323 nm and a less intense broad band in the range of 400–500 nm. Compared with the PPYT polymer, the peak at 323 nm of the PPYT/rGO nanocomposite shows a redshift instead of a blueshift after baseline correction, indicating that the shift of the absorption is due to the interactions between the PPYT and the rGO at the ground state, rather than a simple mathematical superposition of the absorption peaks of the two components. At the PPYT/rGO ratio of 4/1, after baseline correction, the absorption band shows a redshift of 2 nm, from 323 to 325 nm. The PPYTQ polymer exhibits three main absorption peaks at 239, 315, and 539 nm, respectively. With the increase

of the rGO ratio, a 5 nm redshift can be observed from 539 to 544 nm while the other peaks remain unchanged. In contrast, the tPPYT showed a different behavior when the rGO was added. The major absorption bands can be found at 338 and 471 nm for the tPPYT polymer. As the concentration of the rGO increases, the bands remain consistent at 338 and 471 nm after baseline correction. The difference in the UV titration measurement is due to the different conformations of the three polymers on the rGO in ethanol. The rigid planar structures of the PPYT and PPYTQ polymers allow them to interact well with the rGO. However, the tPPYT polymer consumes more energy on preorganization due to the existence of dihedral angel between the adjacent units, which makes the π interaction between the tPPYT and the rGO less preferable.

Density functional theory (DFT) calculations are employed to predict the properties and the interactions between the three polymers and the rGO. The calculated frontier orbital of the PPYT, PPYTQ, and tPPYT is displayed in **Figure 2**a. The gap between the highest occupied molecular orbital (HOMO) and the lowest unoccupied molecular orbital (LUMO) of the tPPYT is calculated to be 2.15 eV, indicating its lower intrinsic electrical conductivity. In addition, the lower LUMO energy level of the tPPYT (−3.23 eV) and the PPYTQ (−2.90 eV) suggests a higher electron affinity, implying a higher reduction potential. As shown in Figure 2b–d, all the polymers prefer (near) AB stacking (half of the atoms in the upper unit lie over the center of a hexagon in graphene) due to the existence of quadrupole of the aromatic system. The adsorption energy of the three polymers is calculated and displayed in Table S2, Supporting Information. Among the three polymers, the PPYTQ shows a more negative

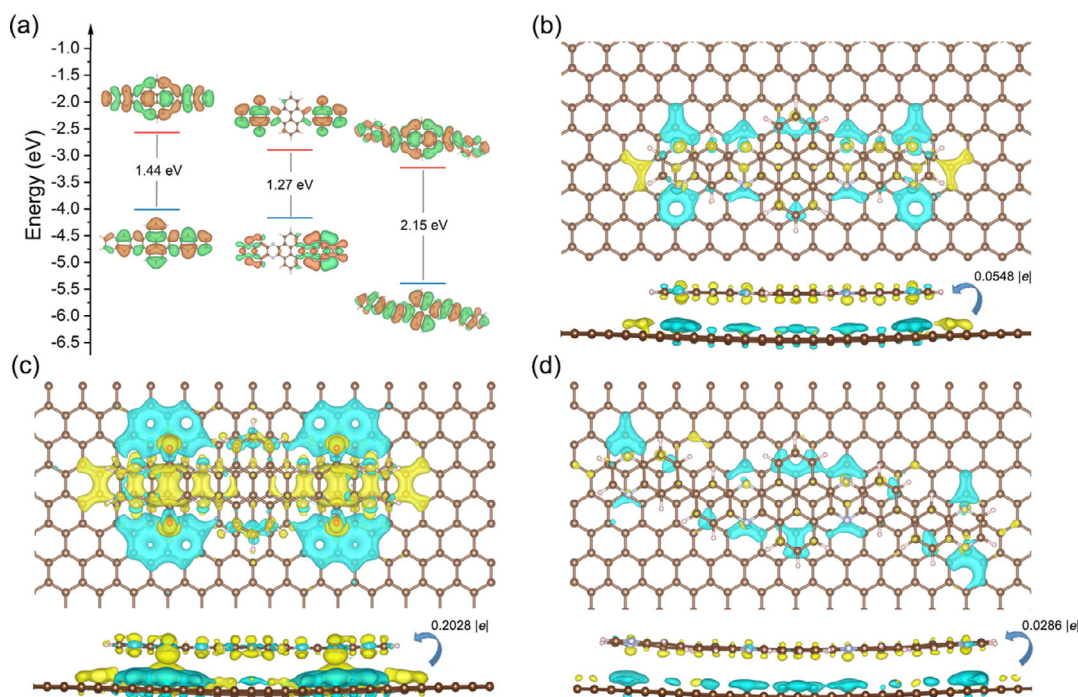**Figure 2.** a) HOMO-LUMO plots of the 1.5 units of the PPYT, PPYTQ, and tPPYT. b–d) The schemcatic diagram of AB stacking between the 1.5 units of the PPYT, PPYTQ, tPPYT, and the rGO; The charge density difference diagram showing the charge transfer between the 1.5 units of the PPYT, PPYTQ, tPPYT, and the rGO. Isosurface value = 0.0002, cyan area: electron accumulation, yellow area: electron depletion.

**ADVANCED
SCIENCE NEWS**

www.advancedsciencenews.com

**ADVANCED
ENERGY & SUSTAINABILITY
RESEARCH**
Open Access

www.advenergysustres.com

normalized adsorption energy (−0.0576 eV), demonstrating a more favored stacking process and a stronger coupling strength. Furthermore, the electrochemical performance is related to the charge transfer between the conducting polymers and the rGO. Figure 2b–d shows the calculated electron transfer process by charge density difference diagram. In the case of 1.5 polymer units, the PPYTQ demonstrates a transfer of 0.2028 electrons, whereas the PPYT and tPPYT can only transfer 0.0548 and 0.0286 electrons, respectively. This disparity suggests that electron transfer is more efficient between the PPYTQ and the rGO. The results also indicate that the twisted structure of the tPPYT hinders its interaction with the rGO, resulting in a decrease in the electrochemical performance of the tPPYT/rGO nanocomposite.

The elemental compositions of the PPYT/PPYTQ/tPPYT polymer and their corresponding 2/1 nanocomposites with the rGO were investigated by XPS. As shown in Figure S5, Supporting Information, all the samples show a major C1s peak and a distinct O1s peak. In addition, with the existence of the pyrazine units, the N1s can also be observed as weaker peaks among the polymers and the corresponding nanocomposites. The rGO shows a C content of 88.2% and an O content of 11.8% (Table S3, Supporting Information). The PPYT polymer possesses a C content of 80.0% and a N content of 7.0% since it contains two pyrazines in one unit. After the combination of the PPYT with the rGO at a ratio of 2/1, the N content decreased to 6.8%, while the O content decreased to 8.9%. The PPYTQ polymer shows a higher O content of 13.0% and a N content of 11.5% since there are two pyrazine rings and two carbonyl groups in a single unit. Compared with the PPYTQ, the 2/1 PPYTQ/rGO

nanocomposite shows approximately the same O content of 13.6% and a lower N content of 8.4%. The tPPYT polymer shows a lower N content (7.8 %) since it contains 28 C atoms in one unit alongside two pyrazine rings. A decreasing trend in the N content can also be seen in the nanocomposite of the tPPYT. **Figure 3**a shows the high-resolution C1s spectrum of the rGO.[61] The C1s peak can be deconvoluted into four peaks at 284.8, 285.7, 287.4, and 288.7 eV with an area ratio of 54.1%, 35.4%, 7.0%, and 3.5%, corresponding to C=C, C—O, C=O, and O=C—O, respectively. As shown in Figure 3b, the deconvolution of the polymers and the corresponding composites shows an additional peak at 285.8 eV (C=N), while the polymers do not display the C—O peaks at 285.7 eV. Interestingly, 3%–5% of the O = C—O peak can be observed in all the polymer samples, which might be attributed to the trapped acetic acid due to the protonation of the pyrazine units. This scenario can also explain the existence of the O1s peak in the PPYT and tPPYT, in which the structures do not contain any O atom. The corresponding N1s spectra can be deconvoluted into 2 significant peaks at 399.6 and 400.7 eV, further confirming the existence of the protonated pyrazine units (Figure S6, Supporting Information). The PPYTQ polymer exhibits a lower protonation ratio (14.5%) compared with the other two polymers since the carbonyl groups decrease the electron density on the nitrogen atoms, leading to a lower proton affinity. Furthermore, the elemental content analysis of each composite reveals a decrease in the percentage of the C=N and C—O bonds in the C1s spectra, while the protonated N remains consistent. This observation is consistent with the expected structural compositions of the rGO and the conductive polymers (Figure 3c).
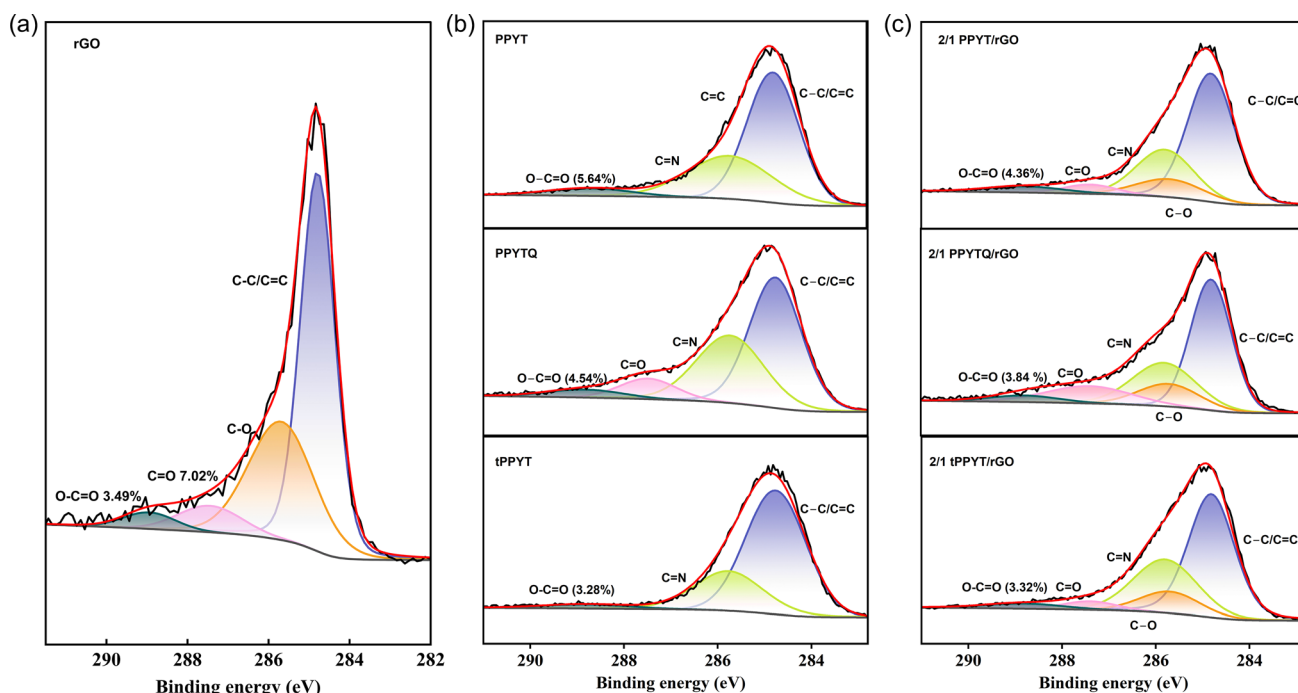

Figure 3. High-resolution X-ray photoelectron spectroscopy (XPS) spectra and the deconvolution of the rGO, three polymers, and the corresponding 2/1 nanocomposites. (a) C1s spectrum of the rGO and b) C1s spectra of the PPYT, PPYTQ, tPPYT polymers. c) C1s spectra of the corresponding 2/1 nanocomposites with the rGO.
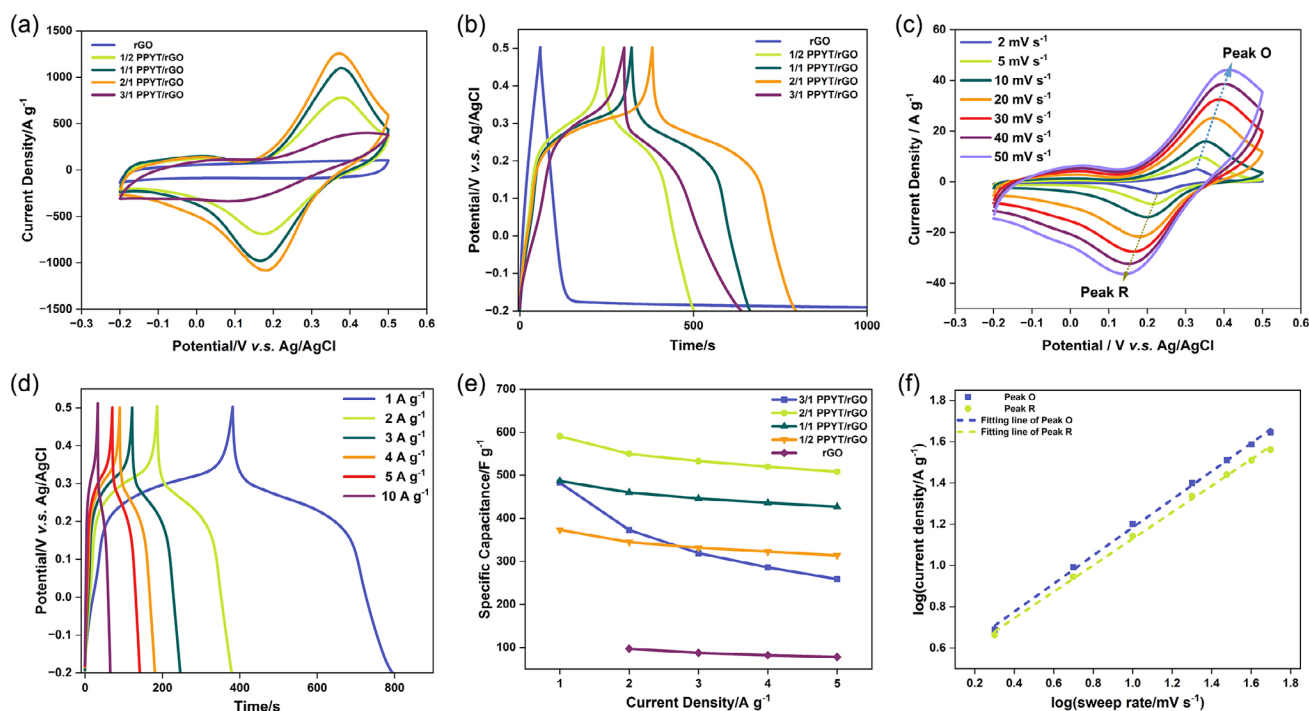
Figure 4. Electrochemical characterization of the PPYT/rGO electrodes at different ratios in a three-electrode system. a) Cyclic voltammetry (CV) curves of the rGO and the PPYT/rGO electrodes at 20 mV s⁻¹. b) GCD curves of the 2/1 PPYT/rGO electrode at various current densities. c) CV curves of the 2/1 PPYT/rGO electrode at different scan rates. d) GCD curves at various current densities. e) The specific capacitance of the rGO and the PPYT/rGO electrodes at different current densities. f) log (*i*) versus log (*ν*) plots according to the CV curves.

2.2. Electrochemical Measurement of the Cathode

Electrochemical measurement was performed in a three-electrode system in a 1 M H_2SO_4 electrolyte to evaluate the electrochemical performance of the cathodes. The CV curves of the rGO and the PPYT/rGO electrodes (including 1/2, 1/1, 2/1, and 3/1 PPYT/rGO ratios) at a scan rate of 20 mV s⁻¹ are shown in **Figure** 4a. The CV curve of the rGO electrode exhibits a typical rectangular shape, illustrating an electrical double-layer energy storage behavior. The pseudocapacitive PPYT polymer in the PPYT/rGO electrodes introduces a pair of redox peaks at ≈0.38/0.18 V (versus Ag/AgCl), which can be attributed to the pyrazine unit, endowing the CV curves a large area. The increased area can imply a higher capacity of the electrodes. The same trend can also be seen among the GCD curves that are shown in Figure 4b. When charging and discharging at the current density of 1 A g⁻¹, the rGO electrode shows almost a symmetric triangle-shaped GCD curve. A longer discharge time was observed with the increase of the ratio of the PPYT polymer (except for the ratio of 3/1), with a contribution from the discharge plateau corresponding to the redox behavior. Furthermore, among all the different ratios, the 2/1 PPYT/rGO electrode exhibits the longest discharge time, demonstrating the most favorable performance.

Three-electrode system testing was employed to investigate the electrochemical performance of the optimized electrode. Figure 4c shows the CV curves of the 2/1 PPYT/rGO electrode at different scan rates from 2 to 50 mV s⁻¹. With the increase of the scan rate, the redox peaks shift toward both more positive and

more negative potentials, attributed to the charge transfer between the PPYT and the rGO.[62] Even at a high scan rate of 50 mV s⁻¹, the CV curve can still remain well-defined and symmetric, indicating high chemical stability and excellent reversibility. Moreover, GCD measurement was conducted to investigate the specific capacitance of the 2/1 PPYT/rGO electrode at 1–5 A g⁻¹ (Figure 4d). A symmetric shape can be seen at each current density of the GCD curve, demonstrating the kinetic reversibility during the redox reaction in the 2/1 PPYT/rGO electrode. The optimized 2/1 PPYT/rGO electrode exhibits the highest specific capacity of 591, 550, 533, 520, and 508 F g⁻¹ at 1–5 A g⁻¹, respectively. Even at a current density of 50 A g⁻¹, it can still exhibit a specific capacity of 235 F g⁻¹ (Figure S7, Supporting Information). It is notable that at a current density of 5 A g⁻¹, the 2/1 PPYT/rGO electrode can still show an 86% retention of the specific capacitance compared to 1 A g⁻¹, indicating excellent rate performance. In addition, the rate performance of the electrodes at different ratios is displayed in Figure 4e. It can be seen that the specific capacity decreases as the graphene mass ratio increases, except for the ratio of 3/1.

To further investigate the charge transfer mechanism of the 2/1 PPYT/rGO electrode, the relationship between the scan rate/mV s⁻¹ and the peak current density/A g⁻¹ is plotted based on the formula $i = av^b$ ($\log(|i|) = b \log(v) + \log(a)$). The *b* value corresponds to the slope of the $\log(|i|) - b\log(v)$ (Figure 4f). If $b = 1$, the charge storage process is dominated by surface-controlled reactions. If $b = 0.5$, diffusion-controlled reactions will dominate the process.[63] Herein, the *b* values of 2/1 PPYT/rGO electrode are 0.68 and 0.64, which are close to 0.5, indicating that

diffusion-controlled reactions dominate the charge storage process. To evaluate the capacitive process contribution at a certain scan rate, the following equation is used

$$i = k_1 v + k_2 v^{1/2} \tag{1}$$

In this equation, $k_1 v$ represents the capacitive-controlled reaction, while $k_2 v^{1/2}$ represents the diffusion-controlled reaction. The surface contribution of the PPYT/rGO electrode at various scan rate from 2 to 50 mV s^{-1} is shown in Figure S8, Supporting Information. From 2 to 10 mV s^{-1}, the capacitive-controlled reaction and the diffusion-controlled reaction almost contribute equally.

The PPYTQ polymer, which possesses more redox sites, is also evaluated by a three-electrode system in 1 M sulfuric acid. **Figure 5**a shows the CV curves of both the rGO and PPYTQ/rGO electrodes at different ratios, encompassing rGO, 1/2, 1/1, 2/1, and 3/1 PPYTQ/rGO. After mixed with the pseudocapacitive PPYTQ polymer, two pairs of redox peaks at ≈0.26/0.13 and 0.34/0.22 V versus Ag/AgCl were observed from the redox reactions of the C=N and the C=O groups (Figure S9, Supporting Information). With the existence of these redox peaks, the CV curves can encircle a larger integrated area which implies a higher capacity. When the ratio of the PPYTQ increases to 2/1, the integrated area of the CV curve reaches to the maximum. The GCD curves of the rGO and the PPYTQ/rGO electrodes at 1 A g^{-1} are shown in Figure 5b. What is particularly notable in this figure is the consistent rise in specific capacity as the discharge time is extended, correlating with the increase of the PPYTQ/rGO ratio, except for the ratio of 3/1. The rGO

electrode shows a triangle-shaped GCD curve with a capacitance of 93.7 F g^{-1}, while the GCD curves of the PPYTQ/rGO electrodes exhibit a contorted shape due to the pseudocapacitive behavior from the redox-active PPYTQ polymer.

The electrochemical performance of the PPYTQ/rGO electrode is further investigated by CV and GCD measurement based on the optimized composite ratio (2:1). Figure 5c shows the CV curves at various scan rates (2–50 mV s^{-1}). With the increase of the scan rate, the two pairs of redox peaks slightly shifted toward more positive and more negative potentials due to the charge transfer between the PPYTQ and the rGO. At a scan rate of 50 mV s^{-1}, the CV curve maintains its shape, indicating outstanding reversibility. The specific capacitance of each electrode can be calculated based on the discharge time at different current densities (1–5 A g^{-1}) in Figure 5d. The 2/1 PPYTQ/rGO electrode shows a specific capacitance at 603, 511, 470, 447, and 418 F g^{-1} at the current density of 1–5 A g^{-1}. At 5 A g^{-1}, the electrode shows a 69% retention of the specific capacity compared with the one at 1 A g^{-1}, which shows a lower rate performance than the 2/1 PPYT/rGO electrode. At 50 A g^{-1}, the electrode can still retain a specific capacitance at 172 F g^{-1} (Figure S10, Supporting Information). The rate performance of the electrodes at different polymer/graphene weight ratios is displayed in Figure 5e. The composite electrode with a higher polymer weight ratio shows a more significant extinction on the specific capacity due to the increase of the current density, except for the ratio of 3/1. Moreover, the b values of the 2/1 PPYTQ/rGO electrode are 0.79, 0.78, 0.78, and 0.84 (Figure 5f), indicating that both
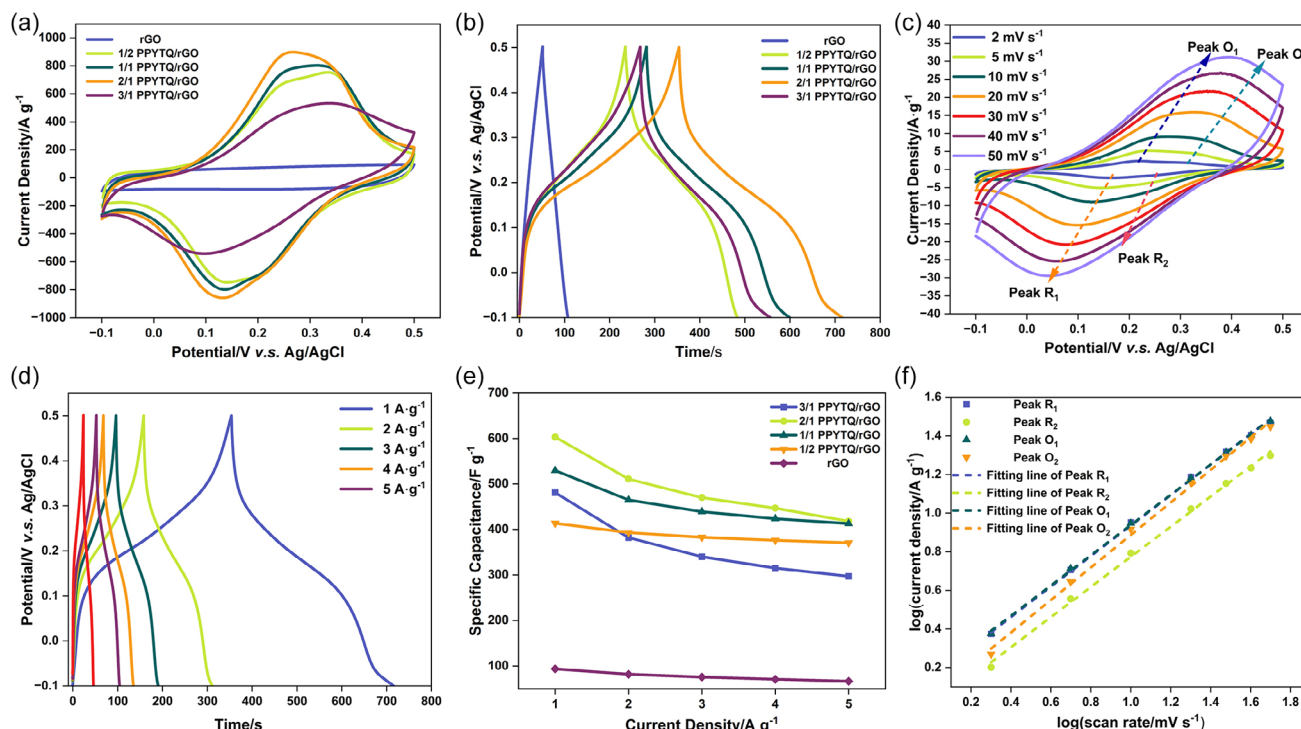

Figure 5. Electrochemical characterization of the rGO and the PPYTQ/rGO electrodes at different ratios in a three-electrode system. a) CV curves of the rGO and the PPYTQ/rGO electrodes at 20 mV s^{-1}. b) GCD curves of the 2/1 PPYTQ/rGO electrode at different current densities. c) CV curves of the 2/1 PPYTQ/rGO electrode at different scan rates. d) GCD curves of the rGO and the PPYTQ/rGO electrodes at different current densities. e) The specific capacitance of the rGO and the PPYTQ/rGO electrodes at different current densities. f) log (*i*) versus log (*v*) plots according to the CV curves.

diffusion-controlled and surface-controlled reactions exist in the charge storage mechanism. As shown in Figure S11, Supporting Information, the capacity contribution of the 2/1 PPYTQ/rGO electrode is similar to the PPYT/rGO electrode. The capacitive contribution increases from 51.4% to 85.7% with the increase of the scan rate from 2 to 50 mV s^{-1}.

For comparison, the tPPYT composite electrode is also evaluated by a three-electrode system under the same condition. The 2/1 tPPYT/rGO electrode shows a narrow operation voltage window (−0.2–0.1 V), while the tPPYT polymer has a limited contribution to the specific capacity due to the weak interaction between the tPPYT polymer and the rGO (Figure S12, Supporting Information). Meanwhile, the electrochemical impedance spectroscopy of the rGO, 2/1 PPYT/rGO, and 2/1 PPYTQ/rGO electrodes was also conducted (Figure S13, Supporting Information). All the Nyquist plots of the samples consist of semicircles in the high-frequency region and sloping lines in the low-frequency area. The sharp rise in the imaginary part of the curves in the low-frequency region suggests the low-proton diffusion impedance and capacitive behavior.[64] In the high-frequency region, the intersection point on the real X-axis represents the electrode resistance (R_s), including the electrical resistance of the active material, the interfacial resistance between the carbon paper and the active material, and the ohmic resistance of the electrolyte.[65] In addition, the diameter of the semicircle in the middle-frequency region corresponds to the charge-transfer resistance (R_{ct}).[66] Compared with the rGO, the composite electrodes show a lower R_{ct} value,[67] indicating that the composite electrodes have better wettability than the rGO electrode at the interface of the electrode (Table S4, Supporting Information). Besides, the 2/1 PPYTQ/rGO electrode and the 2/1 PPYTQ/rGO electrode have almost the same electrode resistance R_s.

Compared to other conducting polymer cathodes reported (as listed in Table S7 of the Supporting Information), the PPYT(Q)/rGO composite electrode emerges as a robust contender. This is attributed to its well-thought-out structural design and optimized component ratio, rendering it a highly competitive cathodic material.

2.3. Characterization and Electrochemical Test of the A-Ti$_3$C$_2$T$_x$ as the Anode

To match with the 2/1 PPYT(Q)/cathode, the A-Ti$_3$C$_2$T$_x$ was prepared by the thermal treatment of the Ti$_3$C$_2$T$_x$ under argon atmosphere. The Ti$_3$C$_2$T$_x$ nanosheets were obtained by the etching the Ti$_3$AlC$_2$ precursor with LiF/HCl (Figure S14, Supporting Information). After calcination, the A-Ti$_3$C$_2$T$_x$ can still retain the sheet-like structure, which guarantees good electrical conductivity. The XRD pattern shows that after exfoliation, the (002) diffraction peak shifted from 9.6° to 7.0°, indicating a larger interlayer distance due to the replacement of aluminum with fluorine or oxygen (Figure S15, Supporting Information). XPS measurement was conducted to further investigate the change in elements for the A-Ti$_3$C$_2$T$_x$. The survey scan spectra are shown in Figure S16, Supporting Information, and the main composition of the Ti$_3$C$_2$T$_x$ nanosheets is C, O, F, and Ti, indicating that aluminum is completely removed during the etching process. Interestingly, the F content decreases from 11.0% to 7.4% during the calcination, while the Ti content decreases from 24.7% to 20.5%, leading to an increase of the C content (Table S8, Supporting Information). As an electrochemical inert group, the F atoms occupy the facial active site on the Ti$_3$C$_2$T$_x$ surface, which is unfavorable to the electrochemical performance.[68] **Figure 6**a shows the high-resolution spectra of Ti 2p. The five peaks at 455.3, 456.2, 457.3, 459.2, and 460.4 eV can be
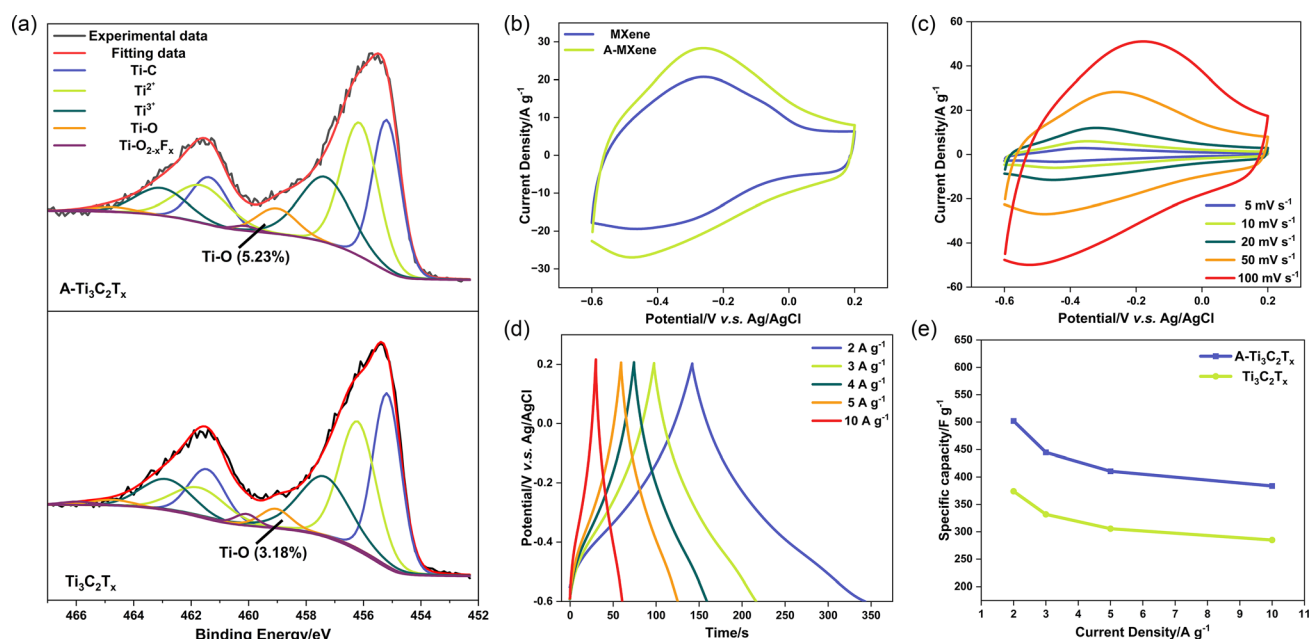

Figure 6. a) The high resolution of Ti 2p XPS spectra of the Ti$_3$C$_2$T$_x$ and the A-Ti$_3$C$_2$T$_x$. b) CV curves of the Ti$_3$C$_2$T$_x$ and the A-Ti$_3$C$_2$T$_x$ at 50 mV s^{-1}. c) CV curves of the Ti$_3$C$_2$T$_x$ and the A-Ti$_3$C$_2$T$_x$. d) GCD curves of the A-Ti$_3$C$_2$T$_x$ at the current density of 2–10 A g^{-1}. e) The specific capacity at various current densities.

**ADVANCED
SCIENCE NEWS**

www.advancedsciencenews.com

**ADVANCED
ENERGY & SUSTAINABILITY
RESEARCH**

www.advenergysustres.com

attributed to Ti—C, Ti^{2+}, Ti^{3+}, Ti—O, and $TiO_{2-x}F_x$, respectively.[69] In addition, the Ti—O content increased from 3.18% to 5.23%, which may be attributed to the oxidation during the calcination. Introducing Ti—O bonds can increase the redox sites on the surface of A-$Ti_3C_2T_x$, allowing better pseudo capability.

The electrochemical properties of the $Ti_3C_2T_x$ and the A-$Ti_3C_2T_x$ electrodes were evaluated by a three-electrode system in a 1 M sulfuric acid electrolyte. The A-$Ti_3C_2T_x$ electrode can encircle a larger CV area compared to the $Ti_3C_2T_x$ electrode at a scan speed of 50 mV s^{-1}, suggesting a higher specific capacity after the heat treatment (Figure 6b). The CV curves of the A-$Ti_3C_2T_x$ at various scan rates are displayed in Figure 6c. The broad redox peaks of the CV curves indicate the pseudocapacitive reactions during the proton insertion. A similar curve shape can be retained even at a rate of 100 mV s^{-1}, demonstrating good redox reversibility and chemical stability. The GCD curves further elucidate the capacity of the A-$Ti_3C_2T_x$ at various current densities (Figure 6d). The distorted triangle-shaped GCD curves demonstrate that the pseudocapacitive behavior predominates the energy storage mechanism. At the current density of 2–10 A g^{-1}, the A-$Ti_3C_2T_x$ exhibits a capacity at 502, 445, 420, 411, and 384 F g^{-1}, respectively. Compared with the $Ti_3C_2T_x$, the A-$Ti_3C_2T_x$ shows a larger specific capacitance at different current densities (Figure 6e).

2.4. ASC Devices

The all-pseudocapacitive 2/1 PPYT(Q)/rGO//A-$Ti_3C_2T_x$ ASCs were assembled using the 2/1 PPYT(Q)/rGO electrode as the cathode and the A-$Ti_3C_2T_x$ as the anode. The full-cell

performance was tested in 1 M H_2SO_4. For the 2/1 PPYTQ/rGO//A-$Ti_3C_2T_x$ ASC device, based on the charge balance formula, the anode and cathode mass ratio are ≈1.1 (the total mass of the cathode and anode is 3.49 mg). **Figure 7**a shows the CV curves of the 2/1 PPYTQ/rGO cathode and the A-$Ti_3C_2T_x$ anode at their operation window, respectively. Both the cathode and the anode exhibit a high capacitance at a scan rate of 10 mV s^{-1}. CV was deployed at various operation windows at a scan rate of 50 mV s^{-1} to determine the operation window of the 2/1 PPYTQ/rGO//A-$Ti_3C_2T_x$ ASC, which is shown in Figure 7b. The CV curve shows a sharp peak when the voltage is over 1.9 V due to the evolution of oxygen on the anode.[70] As a result, the appropriate operation window for the 2/1 PPYTQ/rGO//A-$Ti_3C_2T_x$ ASC is 0–1.9 V. With the optimized operation window in hand, the electrochemical performance of the 2/1 PPYTQ/rGO//A-$Ti_3C_2T_x$ ASC is evaluated by CV at the scan rate of 2–100 mV s^{-1}. The board redox peaks can be observed at all the measured scan rates of 2–100 mV s^{-1} (Figure 7c). As the scan rate increases, the CV curves can retain a similar symmetric shape, indicating good chemical stability and excellent reversibility. The specific capacity of the ASC is further investigated by the GCD curve at a current density of 0.5–10 A g^{-1} (Figure 7d). The curves keep a symmetric curved-triangle shape with the increase of the current density, demonstrating good redox chemical reversibility during the charge/discharge cycles. Furthermore, the ASC shows an excellent specific capacity of 64.1, 59.5, 56.1, 53.9, 52.2, and 46.3 F g^{-1} at the current density of 1–10 A g^{-1} based on the total mass of the cathode and the anode, respectively (Figure 7e). In addition, the cycle life of the ASC is investigated by cyclic charge/discharge at a current density of 5 A g^{-1} (Figure 7f). After 15 000 cycles, all pseudocapacitor

Figure 7. a) CV curves of the 2/1 PPYTQ/rGO and the A-$Ti_3C_2T_x$ electrode at 10 mV s^{-1} based on the three-electrode system. b) CV curves recorded at different potential windows. c) CV curves at different scan rates. d) GCD curves at various current densities. e) Rate performance at 1–10 A g^{-1}. f) Cycle life at 5 A g^{-1}.

**ADVANCED
SCIENCE NEWS**

www.advancedsciencenews.com

**ADVANCED
ENERGY & SUSTAINABILITY
RESEARCH**
Open Access

www.advenergysustres.com

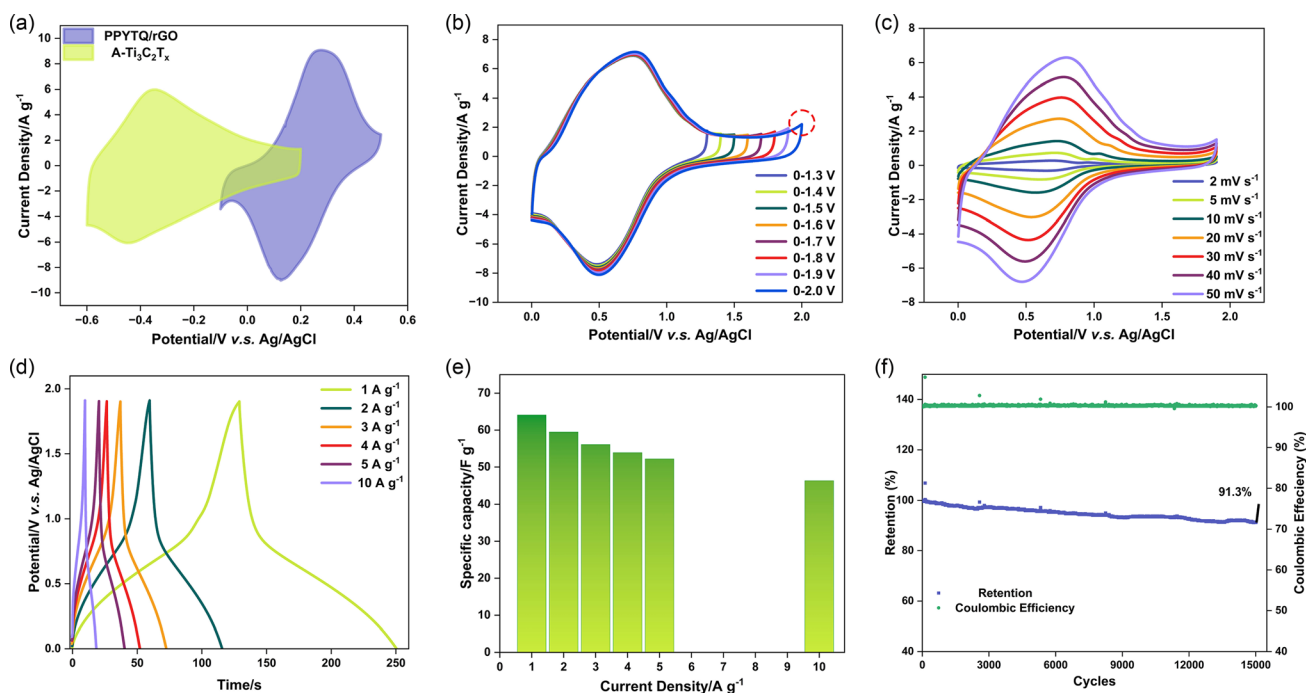**Figure 8.** a) CV curves of the 2/1 PPYT/rGO and the A-Ti$_3$C$_2$T$_x$ electrode at 10 mV s^{-1} based on the three-electrode system. b) CV curves recorded at different potential windows. c) CV curves at different scan rates. d) GCD curves at various current densities. e) Rate performance at 1–10 A g^{-1}. f) Cycle life at 5 A g^{-1}.

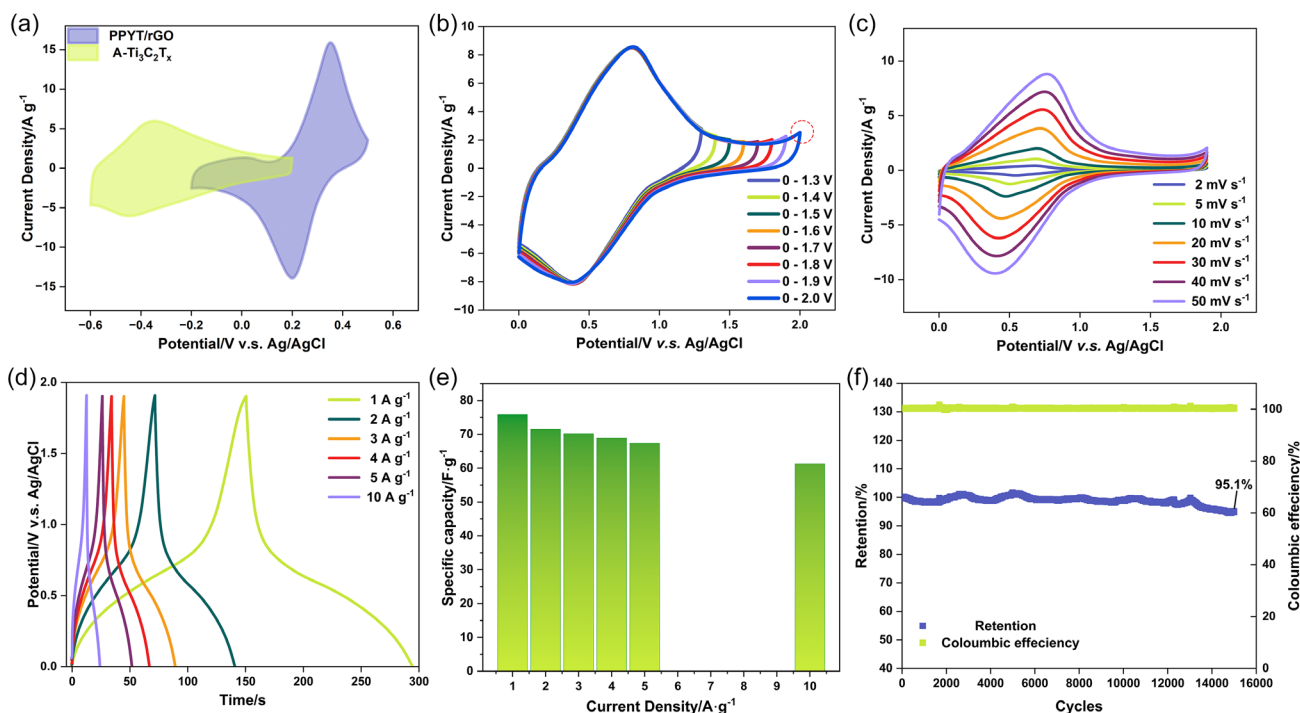shows a 91.3% capacitance retention and a high coloumbic efficiency of ≈100%. The electrode morphology after cyclic charge/discharge was examined through SEM (Figure S17, Supporting Information). Both the composite cathode and the A-Ti$_3$C$_2$T$_x$ anode maintain their sheet-like structures even after 15 000 cycles, demonstrating excellent electrochemical stability.

To compare with the 2/1 PPYTQ/rGO/A-Ti$_3$C$_2$T$_x$ ASC, the 2/1 PPYT/rGO composite electrode was fabricated as the cathode of the ASC and was tested under the same condition. Based on the specific capacitance, the mass ratio of the anode and the cathode is 1.1:1 to balance the charges. **Figure 8**a shows the CV curves of the cathode and the anode at 10 mV s^{-1}. Both the cathode and the anode show an excellent capacity in the operation window, while the CV curve of the PPYT-based cathode can have more overlapping with that of the A-Ti$_3$C$_2$T$_x$ anode compared with the PPYTQ-based cathode. The potential operation window is investigated by CV at a scan rate of 50 mV s^{-1} (Figure 8b). At 2.0 V, a sharp peak can be seen, corresponding to the polarization of water. Therefore, the operating voltage of the 2/1 PPYT/rGO/A-Ti$_3$C$_2$T$_x$ ASC is determined to be 0–1.9 V. In this operation window, the reversible redox peaks can be seen in the scan rate range of 2–100 mV s^{-1} in the CV curves (Figure 8c), indicating good redox reversibility and chemical stability. The symmetric GCD curve at various current densities (Figure 8d) suggests good electrochemical stability and a fast charge/discharge process. The specific capacity at different current densities is displayed in Figure 8e. Based on the mass loading, from 1 to 10 A g^{-1}, the 2/1 PPYT/rGO/A-Ti$_3$C$_2$T$_x$ ASC exhibits an excellent specific capacity of 75.9, 73.1, 70.2, 68.9, 67.5, and 61.4 F g^{-1}.

Furthermore, the 2/1 PPYT/rGO/A-Ti$_3$C$_2$T$_x$ ASC demonstrates excellent cycling capability, maintaining a remarkable retention rate of 95.1% even after 15 000 cycles (Figure 8f). Compared with the freshly fabricated electrode (Figure S17b, Supporting Information), the electrode does not show a significant change in the structure after 15 000 cycles (Figure S17e, Supporting Information).

As shown in **Figure 9** and Table S9, Supporting Information, the PPYT/rGO/A-Ti$_3$C$_2$T$_x$ ASC shows a high energy density of 38.1 Wh kg^{-1} at a power density of 950 W kg^{-1}. It can still retain an eminent energy density of 30.8 Wh kg^{-1} even at a maximum power density of 9500 W kg^{-1}. As for the PPYTQ/rGO/A-Ti$_3$C$_2$T$_x$ ASC device, the energy density can reach 32.1 Wh kg^{-1}. The present device shows much better electrochemical performance compared with other reported organic-based electrodes such as PPy@Ti$_3$C$_2$T$_x$/CC//Ti$_3$C$_2$T$_x$/CC (15.7 Wh kg^{-1}, 620.8 W kg^{-1}),[71] PANI@M-Ti$_3$C$_2$T$_x$/M-Ti$_3$C$_2$T$_x$ (14.8 Wh kg^{-1}, 490 W kg^{-1}),[72] PANI@rGO//Ti$_3$C$_2$T$_x$ (17 Wh kg^{-1}, 200 W kg^{-1}),[73] and rGO/COF-20//rGO/COF-20 (10.3 Wh kg^{-1}, 50 W kg^{-1}).[74]

3. Conclusion

In conclusion, three pyrazine-based pseudocapacitive polymers starting from the 4,5,9,10-pyrenetetrone have been designed and synthesized. The polymers exhibit various interaction behavior on the rGO surface due to the different stereo conformations, which are detected by UV–vis absorption and IR measurement.
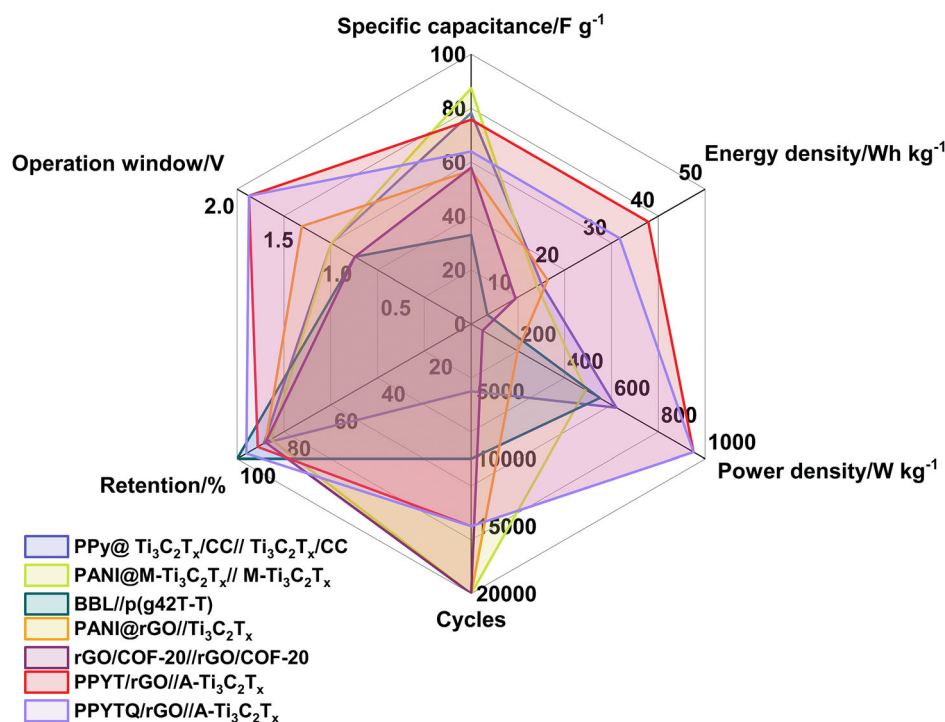
**ADVANCED
SCIENCE NEWS**

www.advancedsciencenews.com

**ADVANCED
ENERGY & SUSTAINABILITY
RESEARCH**

www.advenergysustres.com

Figure 9. A comparison of the electrochemical performance of this work and other ASC devices reported in the literature.

This structure–property relationship is further exhibited in the electrochemical tests. The resulting 2/1 PPYT/rGO composite electrode delivers a high specific capacitance at 591 F g^{-1} at the current density of 1 A g^{-1}, while the 2/1 PPYTQ/rGO electrode shows a specific capacitance at 603 F g^{-1} at the same current density. With the A-Ti$_3$C$_2$T$_x$ as the anode, the 2/1 PPYT/rGO//A-Ti$_3$C$_2$T$_x$ ASC shows an outstanding energy density at 38.1 Wh kg^{-1} at a power density of 950 W kg^{-1}. Even at a power density of 9500 W kg^{-1}, the ASC can still show an energy density of 30.7 Wh kg^{-1}. Meanwhile, the 2/1 PPYTQ/rGO//A-Ti$_3$C$_2$T$_x$ ASC can also show an energy density of 32.1 Wh kg^{-1} at a power density of 950 W kg^{-1}. Both of the ASCs can exhibit more than 90% retention of the capacity after 15 000 cycles. The present study is an important step toward understanding the structure–property relationship between conducting polymers and 2D materials. The ingeniously crafted composite electrodes showcase outstanding overall electrochemical performance. This underscores their potential as advanced energy storage materials for a broad spectrum of applications, including transportation, renewable energy, consumer electronics, and space exploration.

4. Experimental Section

Chemicals and Materials: Lithium fluoride (LiF, >99%), hydrochloric acid (HCl, ≥37%), and tetraminobenzene tetrachloride (98%), 3,3′,4,4′-biphenyl tetramine (98%) were purchased from Sigma-Aldrich. Ti$_3$AlC$_2$ (MAX) and rGO were purchased from Forsman (98%) and Graphenea, respectively.

Preparation of pyrene-4,5,9,10-tetraone and 2,3,5,6-tetraaminoquinone: The two compounds were prepared according to previous reports.[75,76]

Polymerization of PPYT/PPYTQ/tPPYT: To a round bottom flask (100 mL), pyrene-4,5,9,10-tetraone (0.1 mmol, 1 equiv.), tetraminobenzene tetrachloride/3,3′,4,4′-biphenyltetramine/2,3,5,6-tetraaminobenzoquinone/2,3,5,6-tetraaminobenzoquinone (0.11 mmol, 1.1 equiv.), anhydrous toluene (10 mL), and acetic acid (10 mL) were added. The reaction mixture was refluxed in N$_2$ atmosphere for 7 d. The solvent was removed by a rota evaporator. The resulting compound was washed with 5% ammonium carbonate aqueous (20 mL), MilliQ water (20 mL), and ethanol (20 mL each time, multiple times) by sonicating and centrifuging until the supernatant was colorless.

Preparation of Ti$_3$C$_2$T$_x$ and A-Ti$_3$C$_2$T$_x$: The etchant was prepared by adding 12 M LiF (320 mg) to 9 M HCl (4 mL). The solution mixture was stirred with a Teflon magnetic bar for 5 min in a polypropylene centrifuging tube. To this etchant, Ti$_3$AlC$_2$ (200 mg) was added slowly and the mixture was allowed to run for 24 h at 50 °C in an oil bath. After 24 h of stirring, the etched solution was washed repeatedly with water by centrifugating at 4000 rpm for 10 min. At a pH of ≈5–6 (monitored by pH paper), the delamination was started. The dark green supernatant was collected after centrifuging at 4000 rpm for 10 min at 20 °C. This process was repeated four times by adding water and shaking the whole dispersion by hand. All the dispersions were combined, and black solids were obtained after centrifugating at 12 000 rpm for 30 min. Finally, the resulting solid was stored in degassed MilliQ water in a freezer. A-Ti$_3$C$_2$T$_x$ was prepared by annealing the Ti$_3$C$_2$T$_x$ in a tube furnace at 450 °C for 1 h with a heating rate of 5 °C min^{-1} under an argon atmosphere.

Characterization: The morphology of the materials was characterized by SEM (Quanta 200 FEG ESEM). Attenuated total reflectance (ATR) infrared spectra were measured by a PerkinElmer frontier infrared spectrometer. UV–vis absorption spectra were recorded on a Varian Cary 50 Bio UV–vis spectrophotometer. XPS measurement was tested by the PHI 5000 VersaProbe III, and the spectra were processed using the PHI MultiPak software. The electrical conductivity of the as-obtained composites was measured by a four-probe resistivity meter (JANDEL RM3000).

Computational Methods: All DFT calculations were carried out using the Vienna ab initio simulation package with the Perdew–Burke–Ernzerhof functional within the generalized gradient approximation.[77,78] The projector-augmented plane-wave method was employed to describe the ion–electron interactions.[79,80] The cutoff energy was set to 400 eV, and the DFT-D3 method was included to illustrate the van der Waals correction.[81] A Monkhorst–Pack k-point sampling mesh of $2 \times 1 \times 1$ was deployed for geometry optimizations. The energy convergence tolerance was set to be 3×10^{-5} eV. A graphene slab containing 224 carbon atoms was constructed to explore the interaction between the three polymers and the rGO, and all the atoms were allowed to relax. The vacuum space was set to be 20 Å to avoid the interaction between the adjacent layers. Specifically, different adsorption configurations were examined, and the location with the lowest energy was identified and reported.

Electrochemical Measurement: The as-obtained polymers were mixed with rGO and 10 wt% of polyvinylidene fluoride in *N*-methyl-2-pyrrolidone to form a homogeneous slurry. The obtained slurry was cast onto a conductive carbon paper and was further dried at 60 °C in vacuum overnight. The electrodes were named as x/y polymer/rGO (polymer is PPYT/PPYTQ/tPPYT, $x{:}y = 3{:}1$, 2:1, 1:1, and 1:2), where x and y represented the mass ratio between the polymer and the rGO. The mass loading of the polymer/rGO x–y was ≈ 2.08 mg cm^{-2}. All the electrochemical measurement was performed on a Gamry electrochemical potentiostat (1010 E) using a three-electrode test system with a 1 M H$_2$SO$_4$ aqueous solution as the electrolyte. For the three-electrode system, active material-loaded carbon paper is the working electrode, Ag/AgCl in 3 M KCl is the reference electrode, and a platinum gauze is employed as the counter electrode. A three-electrode system was used to test the electrochemical properties of the Ti$_3$C$_2$T$_x$ and the A-Ti$_3$C$_2$T$_x$ in a 1 M H$_2$SO$_4$ aqueous electrolyte. The Ti$_3$C$_2$T$_x$-loaded carbon paper (about 1.5 mg cm^{-2}), Ag/AgCl in 3 M KCl, and activated carbon (around 5 mg cm^{-2}) were employed as the working, reference, and counter electrodes, respectively.

The specific capacitance (C, F g^{-1}) of an electrode was calculated by

$$C = I\Delta t/(m\Delta V) \tag{2}$$

In this equation, I (mA) is the current, Δt (s) is the discharge time, m (mg) is the mass of active materials on the carbon paper, and ΔV (V) is the applied potential.

Two-electrodes system (2/1 PPYT(Q)/rGO//A-Ti$_3$C$_2$T$_x$ ASCs) was assembled by employing the 2/1 PPYT(Q)/rGO electrode as the cathode and the A-Ti$_3$C$_2$T$_x$ as the anode. Moreover, the mass loading of the cathode and the anode can be balanced using the following formula

$$Q^+ = Q^- \tag{3}$$

$$\frac{m^+}{m^-} = C^- V^- / C^+ V^+ \tag{4}$$

The specific capacity of a two-electrode system is calculated based on the total mass loading of the active material on the cathode and on the anode. The corresponding energy density (E, Wh kg^{-1}) and power density (P, W kg^{-1}) of the system were obtained by

$$E = 1/2C(\Delta V)^2 \tag{5}$$

$$P = E \times 3600/\Delta t \tag{6}$$

Here, ΔV (V) and Δt (s) are the working potential and the discharge time.

Supporting Information

Supporting Information is available from the Wiley Online Library or from the author.

Conflict of Interest

The authors declare no conflict of interest.

Data Availability Statement

The data that support the findings of this study are available from the corresponding author upon reasonable request.

[1] P. Simon, Y. Gogotsi, *Nat. Mater.* **2008**, *7*, 845.
[2] M. Shi, P. Das, Z.-S. Wu, T.-G. Liu, X. Zhang, *Adv. Mater.* **2023**, *35*, 2302199.
[3] A. S. Aricò, P. Bruce, B. Scrosati, J.-M. Tarascon, W. van Schalkwijk, *Nat. Mater.* **2005**, *4*, 366.
[4] H. Ye, Y. Li, *Energy Fuels* **2021**, *35*, 7624.
[5] M. Yang, Z. Zhou, *Adv. Sci.* **2017**, *4*, 1600408.
[6] Z. Cao, R. Momen, S. Tao, D. Xiong, Z. Song, X. Xiao, W. Deng, H. Hou, S. Yasar, S. Altin, F. Bulut, G. Zou, X. Ji, *Nano-Micro Lett.* **2022**, *14*, 181.
[7] A. Vlad, N. Singh, C. Galande, P. M. Ajayan, *Adv. Energy Mater.* **2015**, *5*, 1402115.
[8] D. Chao, W. Zhou, F. Xie, C. Ye, H. Li, M. Jaroniec, S.-Z. Qiao, *Sci. Adv.* **2020**, *6*, aba4098.
[9] N. Choudhary, C. Li, J. Moore, N. Nagaiah, L. Zhai, Y. Jung, J. Thomas, *Adv. Mater.* **2017**, *29*, 1605336.
[10] Z. Peng, J. Guo, Q. He, S. Li, L. Tan, Y. Chen, *Sci. China Mater.* **2022**, *65*, 2401.
[11] Z. Peng, A. G. Bannov, S. Li, Y. Huang, L. Tang, L. Tan, Y. Chen, *Adv. Funct. Mater.* **2023**, *33*, 2303205.
[12] T. Guo, D. Zhou, L. Pang, S. Sun, T. Zhou, J. Su, *Small* **2022**, *18*, 2106360.
[13] Q. Abbas, P. Ratajczak, P. Babuchowska, A. L. Comte, D. Bélanger, T. Brousse, F. Béguin, *J. Electrochem. Soc.* **2015**, *162*, A5148.
[14] L. Suo, O. Borodin, T. Gao, M. Olguin, J. Ho, X. Fan, C. Luo, C. Wang, K. Xu, *Science* **2015**, *350*, 938.
[15] S.-E. Chun, B. Evanko, X. Wang, D. Vonlanthen, X. Ji, G. D. Stucky, S. W. Boettcher, *Nat. Commun.* **2015**, *6*, 7818.
[16] Q. Gao, L. Demarconnay, E. Raymundo-Piñero, F. Béguin, *Energy Environ. Sci.* **2012**, *5*, 9611.
[17] X. Lu, L. Li, B. Song, K.-s. Moon, N. Hu, G. Liao, T. Shi, C. Wong, *Nano Energy* **2015**, *17*, 160.

[18] J. Huang, K. Yuan, Y. Chen, *Adv. Funct. Mater.* **2022**, *32*, 2108107.

[19] Y. Shao, M. F. El-Kady, J. Sun, Y. Li, Q. Zhang, M. Zhu, H. Wang, B. Dunn, R. B. Kaner, *Chem. Rev.* **2018**, *118*, 9233.

[20] M. Shi, M. Zhao, L. Jiao, Z. Su, M. Li, X. Song, *J. Power Sources* **2021**, *509*, 230333.

[21] A. K. Geim, *Science* **2009**, *324*, 1530.

[22] A. K. Geim, K. S. Novoselov, *Nat. Mater.* **2007**, *6*, 183.

[23] A. C. Ferrari, F. Bonaccorso, V. Fal'ko, K. S. Novoselov, S. Roche, P. Boggild, S. Borini, F. H. Koppens, V. Palermo, N. Pugno, J. A. Garrido, R. Sordan, A. Bianco, L. Ballerini, M. Prato, E. Lidorikis, J. Kivioja, C. Marinelli, T. Ryhanen, A. Morpurgo, J. N. Coleman, V. Nicolosi, L. Colombo, A. Fert, M. A. Bachtold, G. F. Schneider, F. Guinea, C. Dekker, M. Barbone, et al., *Nanoscale* **2015**, *7*, 4598.

[24] C. Peng, X. Zhang, *Chemistry* **2021**, *3*, 873.

[25] G. Kothandam, G. Singh, X. Guan, J. M. Lee, K. Ramadass, S. Joseph, M. Benzigar, A. Karakoti, J. Yi, P. Kumar, A. Vinu, *Adv. Sci.* **2023**, *10*, 2301045.

[26] R. Shi, C. Han, H. Duan, L. Xu, D. Zhou, H. Li, J. Li, F. Kang, B. Li, G. Wang, *Adv. Energy Mater.* **2018**, *8*, 1802088.

[27] J. S. Seenath, D. Pech, D. Rochefort, *J. Power Sources* **2022**, *548*, 232040.

[28] M. Shi, M. Zhao, Q. Zheng, L. Jiao, Z. Su, M. Li, X. Zhao, X. Song, S. Yang, *Dalton Trans.* **2022**, *51*, 12114.

[29] Z. Peng, S. Li, Y. Huang, J. Guo, L. Tan, Y. Chen, *Adv. Funct. Mater.* **2022**, *32*, 2206539.

[30] M. Mohsen Momeni, H. Mohammadzadeh Aydisheh, B.-K. Lee, *Chem. Eng. J.* **2022**, *450*, 137941.

[31] A. M. Navarro-Suárez, N. Casado, J. Carretero-González, D. Mecerreyes, T. Rojo, *J. Mater. Chem. A* **2017**, *5*, 7137.

[32] M. Shi, C. Peng, X. Zhang, *Small* **2023**, *19*, 2301449.

[33] X. Feng, X. Wu, X. Chen, J. Yuan, S. Lv, B. Ren, X. Sun, E. Liu, S. Tan, P. Gao, *Energy Stor. Mater.* **2021**, *42*, 454.

[34] L. Qin, G. Yang, D. Li, K. Ou, H. Zheng, Q. Fu, Y. Sun, *Chem. Eng. J.* **2022**, *430*, 133045.

[35] Y. Liu, H. Zhou, W. Zhou, S. Meng, C. Qi, Z. Liu, T. Kong, *Adv. Energy Mater.* **2021**, *11*, 2101329.

[36] Z. Su, Y. Jin, H. Wang, Z. Li, L. Huang, H. Wang, *ACS Appl. Energy Mater.* **2022**, *5*, 11915.

[37] F. Vilela, K. Zhang, M. Antonietti, *Energy Environ. Sci.* **2012**, *5*, 7819.

[38] M. Wang, H. Guo, R. Xue, Q. Li, H. Liu, N. Wu, W. Yao, W. Yang, *ChemElectroChem* **2019**, *6*, 2984.

[39] Y. Jiang, Y.-Y. Liu, X. Liu, H. Lin, K. Gao, W.-Y. Lai, W. Huang, *Chem. Soc. Rev.* **2020**, *49*, 5885.

[40] X. Liu, C.-F. Liu, S. Xu, T. Cheng, S. Wang, W.-Y. Lai, W. Huang, *Chem. Soc. Rev.* **2022**, *51*, 3181.

[41] Y. Liao, H. Wang, M. Zhu, A. Thomas, *Adv. Mater.* **2018**, *30*, 1705710.

[42] N. Chen, Y. Ren, P. Kong, L. Tan, H. Feng, Y. Luo, *Appl. Surf. Sci.* **2017**, *392*, 71.

[43] K. Gopalakrishnan, S. Sultan, A. Govindaraj, C. N. R. Rao, *Nano Energy* **2015**, *12*, 52.

[44] G. A. Snook, P. Kao, A. S. Best, *J. Power Sources* **2011**, *196*, 1.

[45] A. M. Bryan, L. M. Santino, Y. Lu, S. Acharya, J. M. D'Arcy, *Chem. Mater.* **2016**, *28*, 5989.

[46] H. Wang, Q. Hao, X. Yang, L. Lu, X. Wang, *ACS Appl. Mater. Interfaces* **2010**, *2*, 821.

[47] Y. Yang, P. Zhang, L. Hao, P. Cheng, Y. Chen, Z. Zhang, *Angew. Chem. Int. Ed.* **2021**, *60*, 21838.

[48] Y. Kou, Y. Xu, Z. Guo, D. Jiang, *Angew. Chem. Int. Ed.* **2011**, *50*, 8753.

[49] M. Mao, C. Luo, T. P. Pollard, S. Hou, T. Gao, X. Fan, C. Cui, J. Yue, Y. Tong, G. Yang, T. Deng, M. Zhang, J. Ma, L. Suo, O. Borodin, C. Wang, *Angew. Chem. Int. Ed.* **2019**, *58*, 17820.

[50] T. Li, X. Yan, Y. Liu, W.-D. Zhang, Q.-T. Fu, H. Zhu, Z. Li, Z.-G. Gu, *Polym. Chem.* **2020**, *11*, 47.

[51] J. M. Seo, H. J. Noh, H. Y. Jeong, J. B. Baek, *J. Am. Chem. Soc.* **2019**, *141*, 11786.

[52] C. Zhang, B. Anasori, A. Seral-Ascaso, S.-H. Park, N. McEvoy, A. Shmeliov, G. S. Duesberg, J. N. Coleman, Y. Gogotsi, V. Nicolosi, *Adv. Mater.* **2017**, *29*, 1702678.

[53] X. Li, Z. Huang, C. E. Shuck, G. Liang, Y. Gogotsi, C. Zhi, *Nat. Rev. Chem.* **2022**, *6*, 389.

[54] J. Zhang, S. Seyedin, S. Qin, Z. Wang, S. Moradi, F. Yang, P. A. Lynch, W. Yang, J. Liu, X. Wang, J. M. Razal, *Small* **2019**, *15*, 1804732.

[55] M. Ghidiu, M. R. Lukatskaya, M.-Q. Zhao, Y. Gogotsi, M. W. Barsoum, *Nature* **2014**, *516*, 78.

[56] Z. Wu, T. Shang, Y. Deng, Y. Tao, Q.-H. Yang, *Adv. Sci.* **2020**, *7*, 1903077.

[57] Z. Lei, Q. Yang, Y. Xu, S. Guo, W. Sun, H. Liu, L.-P. Lv, Y. Zhang, Y. Wang, *Nat. Commun.* **2018**, *9*, 576.

[58] Y. Zhu, P. Chen, Y. Zhou, W. Nie, Y. Xu, *Electrochim. Acta* **2019**, *318*, 262.

[59] L. Xiao, Z. Hu, L. He, L. Jiao, L. Lv, Q. Yin, Q. Wei, Z. Li, Y. Yang, *ACS Appl. Energy Mater.* **2023**, *6*, 68.

[60] C. Zhu, S. Guo, Y. Fang, S. Dong, *ACS Nano* **2010**, *4*, 2429.

[61] M. Wang, M. Ballabio, M. Wang, H.-H. Lin, B. P. Biswal, X. Han, S. Paasch, E. Brunner, P. Liu, M. Chen, M. Bonn, T. Heine, S. Zhou, E. Cánovas, R. Dong, X. Feng, *J. Am. Chem. Soc.* **2019**, *141*, 16810.

[62] S. Isikli, R. Diaz, *J. Power Sources* **2012**, *206*, 53.

[63] H. Zhang, X. Tang, C. Gu, *J. Mater. Chem. A* **2021**, *9*, 4984.

[64] N. An, Z. Guo, C. Guo, M. Wei, D. Sun, Y. He, W. Li, L. Zhou, Z. Hu, X. Dong, *Chem. Eng. J.* **2023**, *458*, 141434.

[65] J. Yang, S. Gunasekaran, *Carbon* **2013**, *51*, 36.

[66] A. Di Fabio, A. Giorgi, M. Mastragostino, F. Soavi, *J. Electrochem. Soc.* **2001**, *148*, A845.

[67] B.-A. Mei, O. Munteshari, J. Lau, B. Dunn, L. Pilon, *J. Phys. Chem. C* **2018**, *122*, 194.

[68] J. Chen, M. Chen, W. Zhou, X. Xu, B. Liu, W. Zhang, C. Wong, *ACS Nano* **2022**, *16*, 2461.

[69] J. Halim, K. M. Cook, M. Naguib, P. Eklund, Y. Gogotsi, J. Rosen, M. W. Barsoum, *Appl. Surf. Sci.* **2016**, *362*, 406.

[70] T. S. Mathis, N. Kurra, X. Wang, D. Pinto, P. Simon, Y. Gogotsi, *Adv. Energy Mater.* **2019**, *9*, 1902007.

[71] X. Chen, F. Su, Q. Zhou, J. Sun, *Surf. Interfaces* **2021**, *26*, 101393.

[72] K. Li, X. Wang, S. Li, P. Urbankowski, J. Li, Y. Xu, Y. Gogotsi, *Small* **2020**, *16*, 1906851.

[73] M. Boota, Y. Gogotsi, *Adv. Energy Mater.* **2019**, *9*, 1802917.

[74] C. Wang, F. Liu, J. Chen, Z. Yuan, C. Liu, X. Zhang, M. Xu, L. Wei, Y. Chen, *Energy Storage Mater.* **2020**, *32*, 448.

[75] J. Hu, D. Zhang, F. W. Harris, *J. Org. Chem.* **2005**, *70*, 707.

[76] T. Chen, J.-H. Dou, L. Yang, C. Sun, J. J. Oppenheim, J. Li, M. Dincă, *J. Am. Chem. Soc.* **2022**, *144*, 5583.

[77] G. Kresse, J. Hafner, *Phys. Rev. B* **1993**, *47*, 558.

[78] J. P. Perdew, K. Burke, M. Ernzerhof, *Phys. Rev. Lett.* **1997**, *78*, 1396.

[79] P. E. Blöchl, *Phys. Rev. B* **1994**, *50*, 17953.

[80] G. Kresse, D. Joubert, *Phys. Rev. B* **1999**, *59*, 1758.

[81] S. Grimme, *J. Comput. Chem.* **2006**, *27*, 1787.